

Circumstellar Medium of Supernovae as New Probes for Feebly-interacting Particles

Yu Cheng ^{1,*} Chui-Fan Kong ^{2,†} Yen-Hsun Lin ^{3,‡} Meng-Ru Wu ^{3,4,5,§} and Seokhoon Yun ^{6,2,¶}

¹*Department of Physics, Korea Advanced Institute of Science and Technology (KAIST), Daejeon 34141, Korea*

²*Particle Theory and Cosmology Group (PTC), Center for Theoretical Physics of the Universe (CTPU),
Institute for Basic Science, Daejeon 34126, Korea*

³*Institute of Physics, Academia Sinica, Taipei 115, Taiwan*

⁴*Institute of Astronomy and Astrophysics, Academia Sinica, Taipei 106, Taiwan*

⁵*Physics Division, National Center for Theoretical Sciences, Taipei 106, Taiwan*

⁶*Department of Physics, Kyungpook National University, Daegu 41566, Korea*

We propose a novel strategy to probe feebly-interacting particles (FIPs) by exploiting the dense, confined circumstellar medium (CSM) surrounding core-collapse supernovae (CCSNe). FIPs produced in the proto-neutron star can deposit substantial visible energy into the CSM via decay prior to the shock breakout from the progenitor star. This energy injection heats and ionizes the CSM, establishing a FIP-induced photosphere that generates distinctive precursor blackbody emission. Using early-time observations of SN 2023ixf, we translate the non-detection of excessive precursor luminosity into stringent new constraints on MeV-scale dark photons as an exemplary model. Our results significantly extend existing CCSN bounds and exclude previously unexplored regions of parameter space. We further demonstrate that the FIP-induced dust sublimation offers robust diagnostics for future Galactic SNe, opening a new avenue to explore the dark sector.

Introduction.—Core-collapse supernovae (CCSNe) provide promising environments to probe new feebly-interacting particles (FIPs), such as axions, axion-like particles, dark photons, and sterile neutrinos, complementing laboratory searches. The proto-neutron star (PNS) reaches temperatures of $\mathcal{O}(30)$ MeV and nuclear-scale densities, enabling efficient FIP production through its interaction with the Standard Model particles. The produced FIPs can free-stream out and decay or become trapped and diffuse for various SN observables to probe their production and transport [1–70].

The canonical constraint is the SN 1987A cooling bound [4, 6]: effective FIP emission from the PNS would shorten or distort the observed neutrino burst, excluding the parameter space where the FIP luminosity competes with the neutrino luminosity at around 1 sec after the core bounce. Beyond the cooling argument, other SN probes can be competitive or even stronger in different parameter spaces. Excessive energy deposition through FIP decay or absorption into the stellar medium outside the PNS can be constrained by SN explosion energy [19, 32]. Visible decays outside the star’s photosphere can yield prompt γ -ray signals (constrained by the non-detection from SN 1987A [71]), positron injection (leading to Galactic X-ray flux), and the integrated radiative emission from cosmic CCSNe that contribute to the diffuse photon background [10, 16, 18].

However, no studies have considered the impact of FIPs on the common presence of the circumstellar medium (CSM) surrounding most SNe produced by various mass-loss mechanisms from the progenitor stars prior to explosions [72–76], except for a brief discussion in Ref. [77]. The interaction of the SN shock or ejecta with the surrounding CSM leaves imprints on SN lightcurve evolution and spectral features, which in turn, offers a

critical diagnostic of the CSM properties. In particular, recent flash spectroscopy surveys indicate that a significant fraction of type II SNe with red supergiant (RSG) progenitors contains confined dense and slowly moving CSM near the progenitor, signaling enhanced progenitor mass-loss events shortly before explosions [78–81].

Recently, observations of the nearby SN 2023ixf in Messier 101 (NGC 5457) [82–87] have provided a benchmark for this phenomenon. Flash spectroscopy and multi-wavelength modeling of SN 2023ixf have revealed that the SN 2023ixf CSM can be modeled by a two-component structure: an inner dense, confined region embedded within an outer, more standard wind [83, 86–88]. Assuming the density profile of each component follows a typical spherically-symmetric steady-state wind model, $\rho(r) = \dot{M}/(4\pi r^2 v_w)$, where \dot{M} is the mass-loss rate and $v_w \sim 30 - 50$ km s^{−1} is the typical RSG wind velocity [89], the inner and dense CSM ($\lesssim 2 \times 10^{14}$ cm) was associated with an enhanced mass-loss ($\dot{M} \sim 10^{-2} M_\odot \text{ yr}^{-1}$) shortly before the explosion, while the outer wind corresponds to mass ejection of $\dot{M} \sim 10^{-4} M_\odot \text{ yr}^{-1}$. Notably, SN 2023ixf also exhibited significant circumstellar dust at $\sim 10^{15}$ cm that can reprocess the progenitor’s photospheric blackbody (BB) emission from optical to infrared [90–92].

In this *Letter*, we propose a novel method to probe FIPs produced from the PNS using CSM-related observables. The energy deposition from visible FIP decays in the CSM ahead of the shock not only raises the gas temperature and modifies the opacity, but also leads to dust sublimation. This induces a new photosphere within the dense CSM, whose emissions are free from dust reprocessing. A stringent constraint on the FIP parameter space is derived using the reported upper limits for SN 2023ixf prior to shock breakout (SBO). A schematic plot of this

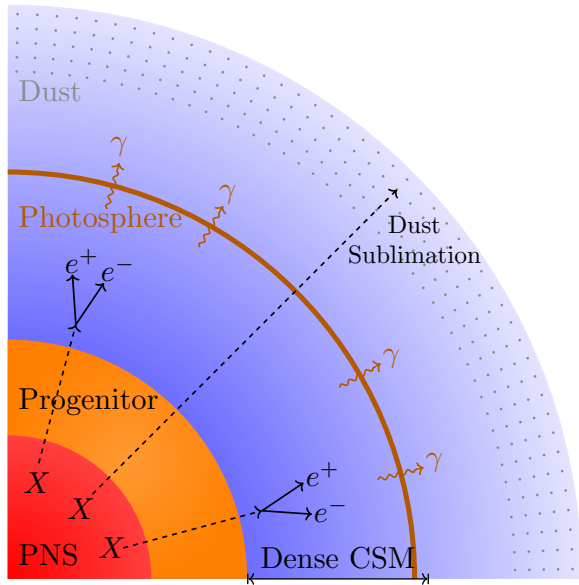


FIG. 1. Schematic plot showing FIPs (X) from the PNS depositing energy into the CSM, forming a new photosphere in dense CSM. The same FIP heating also leads to dust sublimation at the outer CSM, preventing obscuration of the light from the FIP-induced photosphere.

process is shown in Fig. 1.

For the rest of the paper, we specifically consider the dark photon (DP) scenario, in which an additional Abelian gauge boson, denoted by γ' , interacts with the Standard Model through kinetic mixing with the ordinary photon by $\mathcal{L} = (\varepsilon/2)F_{\mu\nu}F'^{\mu\nu}$ in natural unit, where $F_{\mu\nu}^{(\prime)} = \partial_\mu A_\nu^{(\prime)} - \partial_\nu A_\mu^{(\prime)}$ is the photon (DP) field strength tensor and ε is the dimensionless kinetic mixing parameter [93–96]. The ingredients needed for our study, including DP production in the PNS, in-medium effects, and decay, are summarized in Ref. [62] and references therein. In what follows, we adopt the PNS profile obtained from the LS220-s18.88 spherically-symmetric CCSN simulation [97, 98]. For completeness, results using different CCSN simulation profiles are provided in the Supplemental Material (SM). Hereafter we adopt the cgs unit.

DP energy deposition in CSM.—For a DP produced in PNS with momentum k , its decay length reads

$$L_d = \frac{k}{m_{\gamma'}} \Gamma_{\gamma'}^{-1}, \quad (1)$$

where $m_{\gamma'}$ is the DP mass, and $\Gamma_{\gamma'}$ is the DP decay rate in the rest frame. Since DPs emitted from the PNS propagate approximately radially through the CSM, the differential visible energy injection per unit radius reads

$$\frac{dQ}{dr} = \int dk \frac{1}{L_d} \frac{dN_{\gamma'}}{dk} e^{-r/L_d} \sum_i \int dE_i E_i \frac{dN_i}{dE_i}, \quad (2)$$

where $dN_{\gamma'}/dk$ is the DP spectrum integrated over the production volume around the PNS size and over the

emission period (set by the PNS cooling timescale ~ 10 s), and the sum runs over all visible final states $i = e^\pm$. The factor dN_e/dE_e denotes the energy spectrum of e^\pm per DP decay and its explicit expression is given in SM. Hereafter, we focus on the regime where $m_{\gamma'} > 2m_e$ and subdominant channels other than $\gamma' \rightarrow e^\pm$ that produce radiation in the final states are neglected.

For the typical CSM condition, e^\pm from DP decay transfer their kinetic energy to the medium through scattering during their propagation. For e^\pm produced at radius r with initial energy E_e , it loses energy δE_e after traveling over a radial distance δr . We estimate this energy loss using the stopping power table from ESTAR [99] to compute δr for given E_e and δE_e assuming uniform medium mass density ρ . Approximating CSM density as uniform within a shell of thickness $\Delta r \approx r$, we compute the stopping length δr_{stop} as the distance required for e^\pm to come to rest, i.e., $\delta E_{e,r} = E_e - m_e c^2$. For $\delta r_{\text{stop}} \leq \Delta r$, e^\pm deposit all their kinetic energy into the local shell, giving rise to a local energy deposition efficiency $\eta(E_e, r) = \delta E_{e,r}/E_e \simeq 1$ when $E_e \gg m_e c^2$. For $\delta r_{\text{stop}} > \Delta r$, we compute δE_e over $\delta r = \Delta r$ using the same table and take $\eta(E_e, r) = \delta E_e/E_e$. Note that in this case, energy deposition beyond the local shell Δr can occur, but we neglect such non-local effects as a conservative approach. Further details on the stopping-length estimate are provided in the SM.

Since the injected e^\pm energy spectra are determined by the DP spectrum and decay kinematics, we define the spectral-averaged deposition efficiency

$$\bar{\eta}(r) = \frac{\int dE_e \frac{dQ(r)}{dr dE_e} \eta(E_e, r)}{\int dE_e \frac{dQ(r)}{dr dE_e}}. \quad (3)$$

Taking the SN 2023ixf CSM density profile from Ref. [87], shown by the solid blue line in Fig. 2, and assuming the CSM as an ideal gas with a solar-like mass composition of 70% hydrogen, 28% helium, and 2% heavier elements (consisting of 0.6% carbon, 0.6% oxygen, 0.4% nitrogen, and 0.4% iron), we find $\bar{\eta} \simeq 1$ for $r \lesssim 2 \times 10^{14}$ cm for relevant DP parameter space explored here. Beyond this radius, $\bar{\eta}$ drops significantly below 0.1 as the CSM density decreases; see e.g., Fig. 4 in End Matter (EM). The timescale for DP energy deposition can be approximated similarly to Eq. (3) and can be used to estimate the DP heating rate \dot{q}_{heat} . We find that in the region where $\bar{\eta} \simeq 1$, the energy deposition time scale ($\bar{t}_{\text{dep}} \lesssim 1000$ s) is much shorter than the dynamical timescale $t_{\text{dyn}} \sim r/c_s = \mathcal{O}(1-10)$ yrs, where c_s is the local sound speed. Energy deposition from DPs therefore can be considered as instantaneous in inner dense CSM. At outer part, \bar{t}_{dep} can be substantially longer. Detailed evaluation of $\bar{\eta}$, \dot{q}_{heat} and their comparison with the local radiative cooling rate $|\dot{q}_{\text{cool}}|$ are provided in EM.

DP-induced CSM luminosity.—Energy deposition from DP decay can heat the initially cold CSM gas of

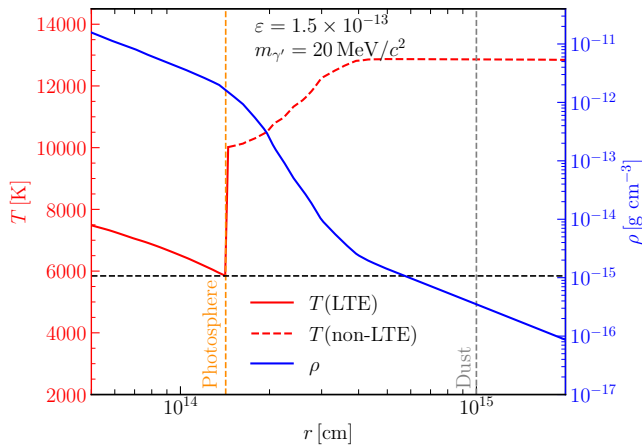


FIG. 2. CSM density profile from Ref. [87] (blue line) features a dense region for $r \lesssim 2 \times 10^{14}$ cm followed by a transition to the outer dilute region. The red line shows the temperature profile following DP energy deposition for the benchmark $(\varepsilon, m_{\gamma'})$. The dashed orange line denotes the DP-induced photosphere at $r_{\text{ph}} \simeq 1.4 \times 10^{14}$ cm and $T_{\text{ph}} \simeq 5800$ K. Estimates show that the CSM reaches the temperature profile shown by the red line in less than ~ 1000 s (see EM).

$\mathcal{O}(10^3$ K) [80, 100] before SBO. To determine the post-heating gas temperature, it is crucial to examine whether radiation is in local thermal equilibrium (LTE) or not. Neglecting the uncertain initial temperature as a conservative approach, we first estimate the post-heating gas temperature T assuming LTE by solving

$$\frac{dQ}{dr} \frac{\bar{\eta}}{4\pi r^2} = u_{\text{gas}} + I_{\text{ion}} + u_{\text{rad}}, \quad (4)$$

where u_{gas} and u_{rad} are the internal energy density of ideal gas and radiation, respectively, and I_{ion} is the ionization energy density. We take $u_{\text{gas}} = (3/2)(n + n_e)k_B T$, where n is the total number density of neutral atoms and ions, $n_e = \sum_i n_i x_i$ is the free-electron density with x_i the ionization fraction for atomic species i determined by solving the Saha equation [101, 102], and k_B is the Boltzmann constant; $I_{\text{ion}} = \sum_i n_i x_i \chi_i$ with χ_i the ionization energy of species i and $u_{\text{rad}} = 4\sigma_{\text{SB}} T^4/c$ with σ_{SB} the Stefan-Boltzmann constant.

Next, we check the validity of the LTE condition by evaluating the Rosseland optical depth $\tau(r) = \int_r^\infty dr \kappa_R(r) \rho(r)$, where the Rosseland mean opacity κ_R is taken from OPAL [103] and Ferguson [104] tables for the high- ($T \geq 10^4$ K) and low-temperature ($T < 10^4$ K) regimes, respectively, with solar-like composition and the obtained T profile assuming LTE. The LTE solution is then only applied to $r < r_{\text{ph}}$, where r_{ph} is the DP-induced new photosphere radius with $\tau(r_{\text{ph}}) = 2/3$. The solid red curve in Fig. 2 shows $T(r)$ in the LTE regime for a benchmark DP parameter set $(\varepsilon, m_{\gamma'}) = (1.5 \times 10^{-13}, 20 \text{ MeV}/c^2)$. The DP-induced photosphere

at $r_{\text{ph}} \simeq 1.4 \times 10^{14}$ cm with the temperature $T_{\text{ph}} \approx 5800$ K, is marked by the vertical orange dashed line. It is worth pointing out that $T_{\text{ph}} \approx 5800$ K is tightly related to the temperature dependence of κ_R . As T increases over 5000 K, κ_R experiences a sharp increase due to H^- formation [105, 106], a prerequisite leading to efficient photon-trapping in dense CSM. Beyond dense CSM ($r \gtrsim 2 \times 10^{14}$ cm), even if a larger ε can heat the region above 5800 K, the low density can not lead to photon-trapping. Our numerical calculations indicate that r_{ph} in $(\varepsilon, m_{\gamma'})$ parameter space consistently locates at $\sim (1-3) \times 10^{14}$ cm, with T_{ph} larger than ~ 5800 K.

Outside r_{ph} where LTE no longer holds, the energy deposition can also heat up the CSM but the radiative cooling needs to be taken into account, whose rate (\dot{q}_{cool}) varies substantially with local gas temperature [107]. We determine the non-LTE gas temperature by taking the lower value from two temperatures obtained by satisfying $\dot{q}_{\text{heat}} = |\dot{q}_{\text{cool}}(T)|$ and by solving Eq. (4) without including I_{ion} and u_{rad} . The dashed red line outside r_{ph} shows the corresponding solution for the benchmark $(\varepsilon, m_{\gamma'})$. The values span between 10000–13000 K. We also note that even in the LTE regime, \dot{q}_{heat} must exceed $|\dot{q}_{\text{cool}}|$ before the gas temperature surpasses 5800 K to trap the radiation; see EM for discussion.

The DP-heated CSM exemplified by Fig. 2 implies a distinct transient emission phase, whose properties qualitatively differ from both the pre-SN stage and the later SBO phase. The elevated gas temperature outside r_{ph} naturally destroys pre-existing CSM dust (likely carbonaceous and silicate grains [90, 92] with a characteristic sublimation temperature $T_{\text{sub}} \sim 2000$ K). As a result, radiation emerging from the newly established photosphere at r_{ph} is expected to be unaffected by dust reprocessing and to resemble a near-BB spectrum with $T_{\text{ph}} \approx 5800$ K. The corresponding BB luminosity reads

$$L_{\text{BB}} \simeq 4\pi r_{\text{ph}}^2 \sigma_{\text{SB}} T_{\text{ph}}^4, \quad (5)$$

which amounts to $\sim 1.6 \times 10^{40}$ erg s $^{-1}$ for the benchmark profile in Fig. 2. We find an emission timescale of ~ 20 hours after the arrival of DPs in the CSM (see EM). This prediction can be confronted with early-time data for SN 2023ixf to derive the constraints presented below.

Constraint from SN 2023ixf.—SN 2023ixf was first reported by K. Itagaki via the Transient Name Server (TNS) [82], and the earliest detection was later confirmed at MJD 60082.85 (20:29 UTC on 18 May 2023). We use extensive archival data, including (non-)detections from amateur astronomers [108], to place the onset of core-collapse at approximately 8–24 hours before the first detection (see EM). We utilize three subsequent non-detections within a 10-hour window (see Fig. 6) following the inferred core-collapse time to set a conservative upper limit on the DP-induced BB luminosity

$$\iota(T_{\text{ph}}) L_{\text{BB}} \leq 8 \times 10^{39} \text{ erg s}^{-1}, \quad (6)$$

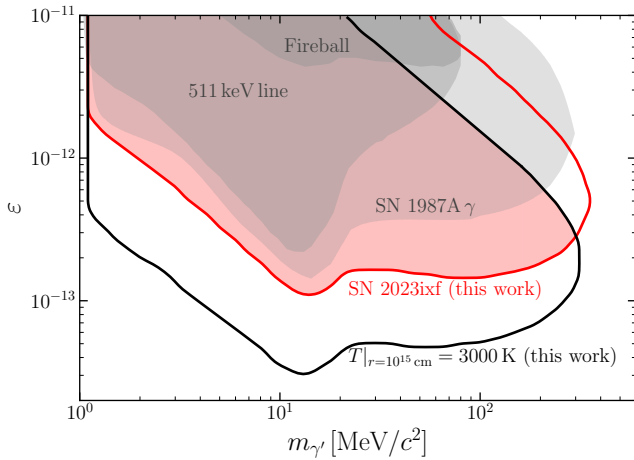


FIG. 3. The solid red contour indicates the parameter that violates Eq. (6) and the solid black curve marks $T|_{r=10^{15} \text{ cm}} > 3000 \text{ K}$. The red-shaded region is robustly excluded. Gray-shaded regions are existing SN constraints adapted from Ref. [62].

where $\iota(T_{\text{ph}}) \simeq 0.54$ accounts for instrument-specific bandwidth sensitivities. This threshold is chosen to accommodate the heterogeneity of amateur telescope configurations and potential systematic uncertainties in the CSM modeling. Further details on the bandwidth-corrected luminosity estimates are provided in EM.

The DP parameter space that violates Eq. (6) is represented by the solid red contour in Fig. 3. Along this contour, the corresponding photospheric temperature is $T_{\text{ph}} \simeq 5800 \text{ K}$ due to the rapidly-rising opacity discussed above, which in turn localizes the photosphere radius to $r_{\text{ph}} \simeq 1.4 \times 10^{14} \text{ cm}$, consistent with Fig. 2. Since the energy density at T_{ph} is dominated by radiation (i.e., $u_{\text{rad}} \gg u_{\text{gas}}, I_{\text{ion}}$), one can estimate the upper limit on total DP energy deposited within r_{ph} as $\sim (4/3)\pi r_{\text{ph}}^3 \times u_{\text{rad}}(T_{\text{ph}}) \sim \mathcal{O}(10^{44}) \text{ erg}$, close to the threshold found numerically

$$Q_{\text{th}} \leq 2.5 \times 10^{44} \text{ erg.} \quad (7)$$

While the DP-heated CSM temperature profile along the lower part of the red contour shares a similar profile as shown in Fig. 2, the upper contour requires further discussion. For larger ε and $m_{\gamma'}$, where the typical DP decay length becomes smaller than the dense CSM radius, the DP energy deposition profile dQ/dr falls off rapidly for $r \gtrsim r_{\text{ph}}$. Consequently, the outer CSM is only weakly heated, so that dust at $r \sim 10^{15} \text{ cm}$ may survive, and the BB emission can be reprocessed into the infrared, weakening the optical constraint. We therefore impose an additional dust-destruction requirement, $T|_{r=10^{15} \text{ cm}} > 3000 \text{ K}$, shown as the solid black contour in Fig. 3. The overlap (red-shaded) region, where the luminosity bound (solid red) intersects this dust-destruction

criterion, is robustly excluded. We also verified that adopting an alternative best-fit CSM density profile from Ref. [83] results in nearly identical exclusion contours. In the remaining region above the black curve but below the red curve, a dedicated treatment of dust sublimation and radiative reprocessing is required for a robust conclusion.

CSM dust sublimation driven by DP heating may provide a powerful diagnostic for the next Galactic (or nearby) CCSN associated with a RSG progenitor, for which CSM dust typically resides at $r \sim 10^{15} \text{ cm}$ [109, 110]. We find that the contour corresponding to $T|_{r=10^{15} \text{ cm}} > 3000 \text{ K}$ is insensitive to the conventional CSM wind profile with $\dot{M} \sim 10^{-6} - 10^{-4} M_{\odot} \text{ yr}^{-1}$. This robustness against variations in \dot{M} and v_w arises from a cancellation in the energy balance in Eq. (4). In the low-density regime ($\bar{\eta} \ll 1$), the deposition efficiency scales as $\bar{\eta} \propto \delta r_{\text{stop}} \propto \rho \propto \dot{M}/v_w$, while the gas internal energy density follows the same scaling, $u_{\text{gas}} \propto n \propto \rho \propto \dot{M}/v_w$. Therefore, in the non-LTE region and neglecting ionization, the required dQ/dr to heat the gas at a given radius to a fixed temperature is approximately independent of \dot{M}/v_w . With low-latency electromagnetic follow-up observation triggered by the neutrino alerts from a nearby SN [111], a rapid spectral transition from infrared-excess to optical/UV dominance between core-collapse and SBO would be a strong indication of dust sublimation by exotic energy injection. Conversely, the absence of such a transition would further strengthen the CSM-based bound on DP as shown by Fig. 3.

Summary and discussion.—We have shown that the CSM surrounding CCSN progenitors and its related observables offer a new avenue to probe FIP. By considering the DP scenario and SN 2023ixf, we have demonstrated that visible energy deposition from DP decay into e^{\pm} pairs can create an optically thick region in a dense CSM, enclosed by a DP-induced photosphere with a temperature $\gtrsim 5800 \text{ K}$, and can additionally sublimate dust in the outer CSM. Together, these effects result in a transient optical signal between core-collapse time and SBO. Exploiting early-time non-detections for SN 2023ixf, we have derived an extended DP constraint beyond the SN 1987A γ bound for $2m_e < m_{\gamma'} \leq 300 \text{ MeV}/c^2$, and quantified the corresponding upper limit on DP energy deposition in the dense CSM of SN 2023ixf [Eq. (7)]. Our results further indicate that the next nearby SN with a RSG progenitor could provide enhanced sensitivity through CSM dust sublimation signatures. We note that the method developed here is generally applicable to other FIP candidates.

More generally, the presence of CSM may impact other existing FIP bounds, particularly those relying on visible decays outside stellar progenitors. Other signatures beyond the simple BB emission discussed in this work, including the detailed spectral line features related to the change of CSM ionization and recombination emission, are well motivated but require dedicated non-LTE

radiative-transfer calculations. The potential impact due to the CSM non-sphericity also merits investigation. Finally, nearby RSGs such as Betelgeuse may provide an attractive testbed for probing FIP-induced dust destruction in a well-characterized stellar environment. We plan to explore all these exciting directions in future work.

Acknowledgments.— We are grateful to Tobias Fischer and Thomas Janka for granting us the use of their SN models. YC is supported by the National Research Foundation of Korea (NRF) Grant RS-2023-00211732, by the Samsung Science and Technology Foundation under Project Number SSTF-BA2302-05, by the POSCO Science Fellowship of POSCO TJ Park Foundation, and by the NRF Grant RS-2024-00405629. CFK and SY are supported by IBS under the project code, IBS-R018-D1. YHL and MRW acknowledge support of the National Science and Technology Council, Taiwan under Grant No. 111-2628-M-001-003-MY4, and the Academia Sinica under Project No. AS-IV-114-M04. MRW also acknowledges support of the Physics Division of the National Center for Theoretical Sciences, Taiwan. CFK and SY thank APCTP, Pohang, Korea for their hospitality during the Focus Program [APCTP-2026-F01] from which this work greatly benefited.

* chengyu@kaist.ac.kr

† kongcf@ibs.re.kr

‡ yenhsun@phys.ncku.edu.tw

§ mwu@as.edu.tw

¶ seokhoon.yun@knu.ac.kr

- [1] G. Raffelt and D. Seckel, *Phys. Rev. Lett.* **60**, 1793 (1988).
- [2] M. S. Turner, *Phys. Rev. Lett.* **60**, 1797 (1988).
- [3] R. Mayle, J. R. Wilson, J. R. Ellis, K. A. Olive, D. N. Schramm, and G. Steigman, *Phys. Lett. B* **203**, 188 (1988).
- [4] G. G. Raffelt, *Phys. Rept.* **198**, 1 (1990).
- [5] H.-T. Janka, W. Keil, G. Raffelt, and D. Seckel, *Phys. Rev. Lett.* **76**, 2621 (1996), [arXiv:astro-ph/9507023](https://arxiv.org/abs/astro-ph/9507023).
- [6] G. G. Raffelt, *Stars as laboratories for fundamental physics: The astrophysics of neutrinos, axions, and other weakly interacting particles* (1996).
- [7] Y. Farzan, *Phys. Rev. D* **67**, 073015 (2003), [arXiv:hep-ph/0211375](https://arxiv.org/abs/hep-ph/0211375).
- [8] G. G. Raffelt and S. Zhou, *Phys. Rev. D* **83**, 093014 (2011), [arXiv:1102.5124](https://arxiv.org/abs/1102.5124) [hep-ph].
- [9] J. B. Dent, F. Ferrer, and L. M. Krauss, (2012), [arXiv:1201.2683](https://arxiv.org/abs/1201.2683) [astro-ph.CO].
- [10] D. Kazanas, R. N. Mohapatra, S. Nussinov, V. L. Teplitz, and Y. Zhang, *Nucl. Phys. B* **890**, 17 (2014), [arXiv:1410.0221](https://arxiv.org/abs/1410.0221) [hep-ph].
- [11] E. Rrapaj and S. Reddy, *Phys. Rev. C* **94**, 045805 (2016), [arXiv:1511.09136](https://arxiv.org/abs/1511.09136) [nucl-th].
- [12] J. H. Chang, R. Essig, and S. D. McDermott, *JHEP* **01**, 107 (2017), [arXiv:1611.03864](https://arxiv.org/abs/1611.03864) [hep-ph].
- [13] E. Hardy and R. Lasenby, *JHEP* **02**, 033 (2017), [arXiv:1611.05852](https://arxiv.org/abs/1611.05852) [hep-ph].
- [14] T. Fischer, S. Chakraborty, M. Giannotti, A. Mirizzi, A. Payez, and A. Ringwald, *Phys. Rev. D* **94**, 085012 (2016), [arXiv:1605.08780](https://arxiv.org/abs/1605.08780) [astro-ph.HE].
- [15] C. A. Argüelles, V. Brdar, and J. Kopp, *Phys. Rev. D* **99**, 043012 (2019), [arXiv:1605.00654](https://arxiv.org/abs/1605.00654) [hep-ph].
- [16] J. Jaeckel, P. C. Malta, and J. Redondo, *Phys. Rev. D* **98**, 055032 (2018), [arXiv:1702.02964](https://arxiv.org/abs/1702.02964) [hep-ph].
- [17] J. H. Chang, R. Essig, and S. D. McDermott, *JHEP* **09**, 051 (2018), [arXiv:1803.00993](https://arxiv.org/abs/1803.00993) [hep-ph].
- [18] W. DeRocco, P. W. Graham, D. Kasen, G. Marques-Tavares, and S. Rajendran, *JHEP* **02**, 171 (2019), [arXiv:1901.08596](https://arxiv.org/abs/1901.08596) [hep-ph].
- [19] A. Sung, H. Tu, and M.-R. Wu, *Phys. Rev. D* **99**, 121305 (2019), [arXiv:1903.07923](https://arxiv.org/abs/1903.07923) [hep-ph].
- [20] P. Carezza, T. Fischer, M. Giannotti, G. Guo, G. Martínez-Pinedo, and A. Mirizzi, *JCAP* **10**, 016 (2019), [Erratum: *JCAP* **05**, E01 (2020)], [arXiv:1906.11844](https://arxiv.org/abs/1906.11844) [hep-ph].
- [21] N. Bar, K. Blum, and G. D’Amico, *Phys. Rev. D* **101**, 123025 (2020), [arXiv:1907.05020](https://arxiv.org/abs/1907.05020) [hep-ph].
- [22] L. Mastrototaro, A. Mirizzi, P. D. Serpico, and A. Esmaili, *JCAP* **01**, 010 (2020), [arXiv:1910.10249](https://arxiv.org/abs/1910.10249) [hep-ph].
- [23] A. M. Suliga, I. Tamborra, and M.-R. Wu, *JCAP* **12**, 019 (2019), [arXiv:1908.11382](https://arxiv.org/abs/1908.11382) [astro-ph.HE].
- [24] P. S. B. Dev, R. N. Mohapatra, and Y. Zhang, *JCAP* **08**, 003 (2020), [Erratum: *JCAP* **11**, E01 (2020)], [arXiv:2005.00490](https://arxiv.org/abs/2005.00490) [hep-ph].
- [25] G. Lucente, P. Carezza, T. Fischer, M. Giannotti, and A. Mirizzi, *JCAP* **12**, 008 (2020), [arXiv:2008.04918](https://arxiv.org/abs/2008.04918) [hep-ph].
- [26] P. Carezza, B. Fore, M. Giannotti, A. Mirizzi, and S. Reddy, *Phys. Rev. Lett.* **126**, 071102 (2021), [arXiv:2010.02943](https://arxiv.org/abs/2010.02943) [hep-ph].
- [27] A. M. Suliga, I. Tamborra, and M.-R. Wu, *JCAP* **08**, 018 (2020), [arXiv:2004.11389](https://arxiv.org/abs/2004.11389) [astro-ph.HE].
- [28] A. Caputo, G. Raffelt, and E. Vitagliano, *Phys. Rev. D* **105**, 035022 (2022), [arXiv:2109.03244](https://arxiv.org/abs/2109.03244) [hep-ph].
- [29] T. Fischer, P. Carezza, B. Fore, M. Giannotti, A. Mirizzi, and S. Reddy, *Phys. Rev. D* **104**, 103012 (2021), [arXiv:2108.13726](https://arxiv.org/abs/2108.13726) [hep-ph].
- [30] A. Sung, G. Guo, and M.-R. Wu, *Phys. Rev. D* **103**, 103005 (2021), [arXiv:2102.04601](https://arxiv.org/abs/2102.04601) [hep-ph].
- [31] F. Calore, P. Carezza, M. Giannotti, J. Jaeckel, G. Lucente, L. Mastrototaro, and A. Mirizzi, *Phys. Rev. D* **105**, 063026 (2022), [arXiv:2112.08382](https://arxiv.org/abs/2112.08382) [hep-ph].
- [32] A. Caputo, H.-T. Janka, G. Raffelt, and E. Vitagliano, *Phys. Rev. Lett.* **128**, 221103 (2022), [arXiv:2201.09890](https://arxiv.org/abs/2201.09890) [astro-ph.HE].
- [33] C. S. Shin and S. Yun, *Phys. Rev. D* **108**, 055014 (2023), [arXiv:2211.15677](https://arxiv.org/abs/2211.15677) [hep-ph].
- [34] S. Hoof and L. Schulz, *JCAP* **03**, 054 (2023), [arXiv:2212.09764](https://arxiv.org/abs/2212.09764) [hep-ph].
- [35] R. Z. Ferreira, M. C. D. Marsh, and E. Müller, *JCAP* **11**, 057 (2022), [arXiv:2205.07896](https://arxiv.org/abs/2205.07896) [hep-ph].
- [36] A. Lella, P. Carezza, G. Lucente, M. Giannotti, and A. Mirizzi, *Phys. Rev. D* **107**, 103017 (2023), [arXiv:2211.13760](https://arxiv.org/abs/2211.13760) [hep-ph].
- [37] S.-Y. Ho, J. Kim, P. Ko, and J.-h. Park, *Phys. Rev. D* **107**, 075002 (2023), [arXiv:2212.01155](https://arxiv.org/abs/2212.01155) [hep-ph].
- [38] M. Diamond, D. F. G. Fiorillo, G. Marques-Tavares, and E. Vitagliano, *Phys. Rev. D* **107**, 103029 (2023), [Erratum: *Phys.Rev.D* **108**, 049902 (2023)],

- arXiv:2303.11395 [hep-ph].
- [39] P. Carena, G. Lucente, L. Mastrototaro, A. Mirizzi, and P. D. Serpico, *Phys. Rev. D* **109**, 063010 (2024), arXiv:2311.00033 [hep-ph].
- [40] E. Müller, P. Carena, C. Eckner, and A. Goobar, *Phys. Rev. D* **109**, 023018 (2024), arXiv:2306.16397 [astro-ph.HE].
- [41] A. Lella, P. Carena, G. Co', G. Lucente, M. Giannotti, A. Mirizzi, and T. Rauscher, *Phys. Rev. D* **109**, 023001 (2024), arXiv:2306.01048 [hep-ph].
- [42] K. Akita, S. H. Im, M. Masud, and S. Yun, *JHEP* **07**, 057 (2024), arXiv:2312.13627 [hep-ph].
- [43] P. De la Torre Luque, S. Balaji, P. Carena, and L. Mastrototaro, *Phys. Rev. D* **111**, L061303 (2025), arXiv:2405.08482 [hep-ph].
- [44] C. A. Manzari, Y. Park, B. R. Safdi, and I. Savoray, *Phys. Rev. Lett.* **133**, 211002 (2024), arXiv:2405.19393 [hep-ph].
- [45] K. Mori, T. Takiwaki, K. Kotake, and S. Horiuchi, *Phys. Rev. D* **110**, 023031 (2024), arXiv:2402.14333 [astro-ph.HE].
- [46] D. F. G. Fiorillo and E. Vitagliano, *Phys. Rev. Lett.* **133**, 251004 (2024), arXiv:2404.07714 [hep-ph].
- [47] V. Syvolap and O. Ruchayskiy, *Phys. Rev. D* **110**, 115043 (2024), arXiv:2404.19191 [hep-ph].
- [48] C. Li, Z. Liu, W. Lu, and Z. Ye, *JHEP* **07**, 116 (2025), arXiv:2408.04953 [hep-ph].
- [49] A. Lella, E. Ravensburg, P. Carena, and M. C. D. Marsh, *Phys. Rev. D* **110**, 043019 (2024), arXiv:2405.00153 [hep-ph].
- [50] K. Springmann, M. Stadlbauer, S. Stelzl, and A. Weiler, *Phys. Rev. D* **112**, 075009 (2025), arXiv:2410.19902 [hep-ph].
- [51] S. Vogl and X.-J. Xu, *JCAP* **07**, 058 (2025), arXiv:2411.18052 [hep-ph].
- [52] D. Alonso-González, D. Cerdeño, M. Cermeño, and A. D. Perez, *Phys. Rev. D* **111**, 083019 (2025), [Erratum: *Phys. Rev. D* **112**, 029901 (2025)], arXiv:2412.09595 [hep-ph].
- [53] J. N. Benabou, C. A. Manzari, Y. Park, G. Prabhakar, B. R. Safdi, and I. Savoray, *Phys. Rev. D* **111**, 095029 (2025), arXiv:2412.13247 [hep-ph].
- [54] E. Hardy, A. Sokolov, and H. Stubbs, *JHEP* **04**, 013 (2025), arXiv:2410.17347 [hep-ph].
- [55] T. Takata, K. Mori, K. Nakamura, and K. Kotake, *Phys. Rev. D* **111**, 103028 (2025), arXiv:2503.09005 [astro-ph.HE].
- [56] A. Caputo, H.-T. Janka, G. Raffelt, and S. Yun, *Phys. Rev. Lett.* **134**, 151002 (2025), arXiv:2502.01731 [hep-ph].
- [57] D. F. G. Fiorillo, T. Pitik, and E. Vitagliano, *Phys. Rev. Lett.* **135**, 071005 (2025), arXiv:2503.13653 [hep-ph].
- [58] C. V. Cappiello, P. S. B. Dev, and A. V. Patwardhan, (2025), arXiv:2503.09691 [hep-ph].
- [59] S. Balaji, P. Carena, P. De la Torre Luque, A. Lella, and L. Mastrototaro, *Phys. Rev. D* **111**, 083053 (2025), arXiv:2501.07725 [hep-ph].
- [60] F. R. Candón, D. F. G. Fiorillo, H.-T. Janka, B. F. A. van Baal, and E. Vitagliano, (2025), arXiv:2509.18253 [hep-ph].
- [61] K. Mori and M. Mori, *JCAP* **11**, 081 (2025), arXiv:2508.18491 [astro-ph.HE].
- [62] A. Caputo, J. Park, and S. Yun, (2025), arXiv:2511.15785 [hep-ph].
- [63] M. Mori and K. Mori, (2025), arXiv:2509.05973 [astro-ph.HE].
- [64] R. Z. Ferreira, M. C. D. Marsh, and E. Ravensburg, (2025), arXiv:2510.14469 [hep-ph].
- [65] A. Gupta and M. Sen, (2025), arXiv:2511.11219 [hep-ph].
- [66] Z.-M. Huang, C. Li, and Z. Liu, (2025), arXiv:2510.22523 [hep-ph].
- [67] N. Blinov, P. J. Fox, K. J. Kelly, R. Plestid, and T. Zhou, (2025), arXiv:2511.09619 [hep-ph].
- [68] M. Joseph, S. Liebersbach, A. A. Madathil, and G. Marques-Tavares, (2026), arXiv:2603.04513 [hep-ph].
- [69] A. Caputo and R. Essig (2026) arXiv:2603.08430 [hep-ph].
- [70] Y. Yu, W. Maitra, P. S. B. Dev, J.-F. Fortin, S. P. Harris, K. Sinha, and Y. Zhang, (2026), arXiv:2603.08695 [hep-ph].
- [71] L. Oberauer, C. Hagner, G. Raffelt, and E. Rieger, *Astropart. Phys.* **1**, 377 (1993).
- [72] N. Smith, *Ann. Rev. Astron. Astrophys.* **52**, 487 (2014), arXiv:1402.1237 [astro-ph.SR].
- [73] P. Chandra, *Space Sci. Rev.* **214**, 27 (2018), arXiv:1712.07405 [astro-ph.HE].
- [74] N. Smith, "Interacting supernovae: Types iin and ibn," in *Handbook of Supernovae* (Springer International Publishing, 2017) p. 403–429.
- [75] M. Fraser, *Royal Society Open Science* **7**, 200467 (2020), <https://royalsocietypublishing.org/rsos/article-pdf/doi/10.1098/rsos.200467/985936/rsos.200467.pdf>.
- [76] L. Dessart, (2024), arXiv:2405.04259 [astro-ph.SR].
- [77] A. Kozyreva, A. Caputo, P. Baklanov, A. Mironov, and H.-T. Janka, *Astron. Astrophys.* **694**, A319 (2025), arXiv:2410.19939 [astro-ph.HE].
- [78] F. Förster *et al.*, *Nature Astron.* **2**, 808 (2018), [Erratum: *Nature Astron.* **3**, 107 (2019)], arXiv:1809.06379 [astro-ph.HE].
- [79] R. J. Bruch *et al.*, *Astrophys. J.* **912**, 46 (2021), arXiv:2008.09986 [astro-ph.HE].
- [80] W. Jacobson-Galán *et al.*, *Astrophys. J.* **924**, 15 (2022), arXiv:2109.12136 [astro-ph.HE].
- [81] R. J. Bruch *et al.*, *Astrophys. J.* **952**, 119 (2023), arXiv:2212.03313 [astro-ph.HE].
- [82] K. Itagaki, "Discovery certificate for object 2023ixf," <https://www.wis-tns.org/object/2023ixf/discovery-cert>.
- [83] W. V. Jacobson-Galan *et al.*, *Astrophys. J. Lett.* **954**, L42 (2023), arXiv:2306.04721 [astro-ph.HE].
- [84] K. A. Bostroem *et al.*, *Astrophys. J. Lett.* **956**, L5 (2023), arXiv:2306.10119 [astro-ph.HE].
- [85] R. S. Teja *et al.*, *Astrophys. J. Lett.* **954**, L12 (2023), arXiv:2306.10284 [astro-ph.HE].
- [86] D. Hiramatsu *et al.*, *Astrophys. J. Lett.* **955**, L8 (2023), arXiv:2307.03165 [astro-ph.HE].
- [87] E. A. Zimmerman *et al.*, *Nature* **627**, 759 (2024), arXiv:2310.10727 [astro-ph.HE].
- [88] W. V. Jacobson-Galán, *Universe* **11**, 231 (2025), arXiv:2507.08078 [astro-ph.HE].
- [89] R. A. Chevalier and C. Fransson, *Astrophys. J.* **420**, 268 (1994).
- [90] C. D. Kilpatrick *et al.*, *Astrophys. J. Lett.* **952**, L23 (2023), arXiv:2306.04722 [astro-ph.SR].
- [91] Z. Niu, N.-C. Sun, J. R. Maund, Y. Zhang, R. Zhao,

- and J. Liu, *Astrophys. J. Lett.* **955**, L15 (2023), [arXiv:2308.04677](https://arxiv.org/abs/2308.04677) [astro-ph.SR].
- [92] J. E. Jencson *et al.*, *Astrophys. J. Lett.* **952**, L30 (2023), [arXiv:2306.08678](https://arxiv.org/abs/2306.08678) [astro-ph.SR].
- [93] B. Holdom, *Phys. Lett. B* **166**, 196 (1986).
- [94] L. B. Okun, *Sov. Phys. JETP* **56**, 502 (1982).
- [95] P. Galison and A. Manohar, *Phys. Lett. B* **136**, 279 (1984).
- [96] N. Arkani-Hamed, D. P. Finkbeiner, T. R. Slatyer, and N. Weiner, *Phys. Rev. D* **79**, 015014 (2009), [arXiv:0810.0713](https://arxiv.org/abs/0810.0713) [hep-ph].
- [97] R. Bollig, N. Yadav, D. Kresse, H. T. Janka, B. Müller, and A. Heger, *Astrophys. J.* **915**, 28 (2021), [arXiv:2010.10506](https://arxiv.org/abs/2010.10506) [astro-ph.HE].
- [98] “Garching core-collapse supernova research archive,” <https://wwwmpa.mpa-garching.mpg.de/ccsnarchive/>.
- [99] “ESTAR program,” <https://physics.nist.gov/PhysRefData/Star/Text/ESTAR.html>.
- [100] L. Dessart, D. J. Hillier, and E. Audit, *Astron. Astrophys.* **605**, A83 (2017), [arXiv:1704.01697](https://arxiv.org/abs/1704.01697) [astro-ph.SR].
- [101] M. N. Saha, *Nature (London)* **105**, 232 (1920).
- [102] M. N. Saha, *Proceedings of the Royal Society of London Series A* **99**, 135 (1921).
- [103] C. A. Iglesias and F. J. Rogers, *Astrophys. J.* **464**, 943 (1996).
- [104] J. W. Ferguson *et al.*, *Astrophys. J.* **623**, 585 (2005), [arXiv:astro-ph/0502045](https://arxiv.org/abs/astro-ph/0502045).
- [105] R. Wildt, *Astrophys. J.* **90**, 611 (1939).
- [106] S. Chandrasekhar, *Astrophys. J.* **102**, 223 (1945).
- [107] K. M. Schure, D. Kosenko, J. S. Kaastra, R. Képens, and J. Vink, *Astron. Astrophys.* **508**, 751 (2009), [arXiv:0909.5204](https://arxiv.org/abs/0909.5204) [astro-ph.GA].
- [108] “Report on SN 2023ixf at the Transient Name Server,” <https://www.wis-tns.org/object/2023ixf/>.
- [109] W. C. Danchi, M. Bester, C. G. Degiacomi, L. J. Greenhill, and C. H. Townes, *Astron. J.* **107**, 1469 (1994).
- [110] T. Verhoelst, N. Van der Zypen, S. Hony, L. Decin, J. Cami, and K. Eriksson, *Astron. Astrophys.* **498**, 127 (2009), [arXiv:0901.1262](https://arxiv.org/abs/0901.1262) [astro-ph.SR].
- [111] S. Al Kharusi *et al.* (SNEWS), *New J. Phys.* **23**, 031201 (2021), [arXiv:2011.00035](https://arxiv.org/abs/2011.00035) [astro-ph.HE].
- [112] G. Li *et al.*, *Nature* **627**, 754 (2024), [arXiv:2311.14409](https://arxiv.org/abs/2311.14409) [astro-ph.HE].
- [113] G. Hosseinzadeh *et al.*, *Astrophys. J. Lett.* **953**, L16 (2023), [arXiv:2306.06097](https://arxiv.org/abs/2306.06097) [astro-ph.HE].
- [114] D. Dickinson *et al.*, *Astrophys. J.* **984**, 71 (2025), [arXiv:2412.14406](https://arxiv.org/abs/2412.14406) [astro-ph.HE].
- [115] Y.-J. Qin, K. Zhang, J. Bloom, J. Sollerman, E. A. Zimmerman, I. Irani, S. Schulze, A. Gal-Yam, M. Kasliwal, M. W. Coughlin, D. A. Perley, C. Fremling, and S. Kulkarni, *MNRAS* **534**, 271 (2024), [arXiv:2309.10022](https://arxiv.org/abs/2309.10022) [astro-ph.SR].
- [116] M. C. Bersten, M. Orellana, G. Folatelli, L. Martinez, M. P. Piccirilli, T. Regna, L. M. R. Aguilar, and K. Ertini, *Astron. Astrophys.* **681**, L18 (2024), [arXiv:2310.14407](https://arxiv.org/abs/2310.14407) [astro-ph.SR].
- [117] K. Zhang, D. Kennedy, B. Oostermeyer, J. Bloom, and D. A. Perley, “Pre-Discovery Images of SN 2023ixf taken at T-[9,18,33] hours,” <https://www.wis-tns.org/astronotes/astronote/2023-125>.
- [118] M. D. Fulton *et al.* (ATLAS), “ATLAS forced photometry pre-discovery limit of SN 2023ixf,” <https://www.wis-tns.org/astronotes/astronote/2023-124>.
- [119] Y. Mao *et al.*, “Onset of SN 2023ixf observed over East Asian longitudes,” <https://www.wis-tns.org/astronotes/astronote/2023-130>.
- [120] O. Yaron, R. Bruch, P. Chen, I. Irani, E. Zimmerman, A. Gal-Yam, and Y.-J. Qin, “Amateur astronomer contribution to constraining the explosion time and rise of the Type II SN 2023ixf in M101,” <https://www.wis-tns.org/astronotes/astronote/2023-133>.
- [121] T. Fischer, S. C. Whitehouse, A. Mezzacappa, F. K. Thielemann, and M. Liebendorfer, *Astron. Astrophys.* **517**, A80 (2010), [arXiv:0908.1871](https://arxiv.org/abs/0908.1871) [astro-ph.HE].

e^\pm energy deposition timescale

The characteristic timescale for an e^\pm to deposit energy locally can be estimated by the stopping length, $t \sim \delta r_{\text{stop}}/c$, as the energy deposition mainly takes place when e^\pm is relativistic. Following the same approach for computing $\eta(E_e, r)$ in the main text, we define the energy deposition timescale as $t_{\text{dep}}(E_e, r) = \min(\delta r_{\text{stop}}, \Delta r)/c$. The spectral-averaged value reads

$$\bar{t}_{\text{dep}}(r) = \frac{\int dE_e \frac{dQ(r)}{dr dE_e} t_{\text{dep}}(E_e, r)}{\int dE_e \frac{dQ(r)}{dr dE_e}}. \quad (8)$$

We show both $\bar{\eta}$ and \bar{t}_{dep} as functions of r for $\varepsilon = 10^{-13}$, 10^{-12} and $m_{\gamma'} = 10 \text{ MeV}/c^2$ in Fig. 4, calculated using Eqs. (3) and (8), respectively. Note that both quantities are only mildly sensitive to the choice of $(\varepsilon, m_{\gamma'})$.

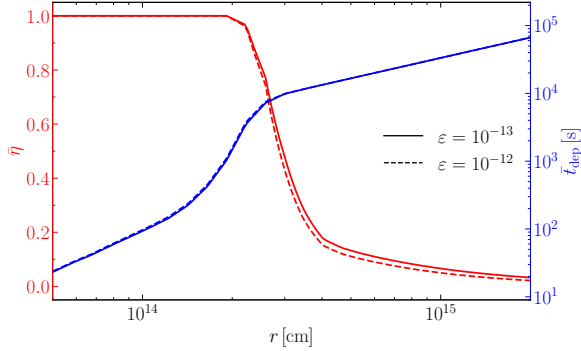


FIG. 4. The spectral-averaged energy deposition efficiency $\bar{\eta}$ (red) and energy deposition time \bar{t}_{dep} (blue) as functions of r for CSM density profile shown in Fig. 2. Two different values of $\varepsilon = 10^{-13}$ (solid) and $\varepsilon = 10^{-12}$ (dashed) are illustrated. Both assume $m_{\gamma'} = 10 \text{ MeV}/c^2$.

Heating/cooling rates and various timescales

Fig. 5 compares the DP heating rate, $\dot{q}_{\text{heat}} = (\bar{\eta}/\bar{t}_{\text{dep}})dQ/dr$ (red), with the radiative cooling rate, $|\dot{q}_{\text{cool}}| = n_{\text{H}}^2 \Lambda(T)$, as functions of radius r for benchmark $(\varepsilon, m_{\gamma'}) = (1.5 \times 10^{-13}, 20 \text{ MeV}/c^2)$. Here, $\Lambda(T)$ is the radiative loss function normalized to n_{H} [107]. We evaluate $|\dot{q}_{\text{cool}}|$ at two representative temperatures: 6000 K (blue) and 12800 K (green); solid lines indicate the regions in which each choice is relevant.

At $r < r_{\text{ph}}$, radiative cooling is only relevant before photon-trapping occurs at $T \gtrsim 5800 \text{ K}$ (see main text). We adopt 6000 K as a conservative value for the maximal radiative cooling rate during the DP-heating phase. Even with this choice, we find that \dot{q}_{heat} exceeds $|\dot{q}_{\text{cool}}|$ by at least a factor of 2.

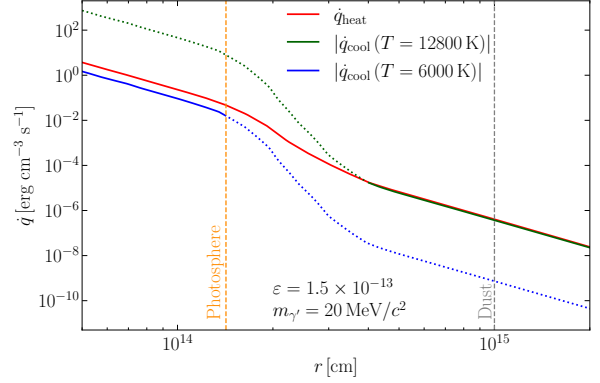


FIG. 5. DP heating rate \dot{q}_{heat} (red) for benchmark $(\varepsilon, m_{\gamma'}) = (1.5 \times 10^{-13}, 20 \text{ MeV}/c^2)$ and the radiative cooling rates $|\dot{q}_{\text{cool}}|$ for $T = 12800 \text{ K}$ (green) and 6000 K (blue); see text for details.

For $r > r_{\text{ph}}$, the gas temperature is determined by the balance condition $\dot{q}_{\text{heat}} = |\dot{q}_{\text{cool}}|$; we denote the corresponding equilibrium temperature by T_{eq} , which is approximately 12800 K for $r \gtrsim 4 \times 10^{14} \text{ cm}$. We notice that for substantially larger ε , \dot{q}_{heat} can become so large that the radiative cooling cannot balance the heating. In that regime, the gas continues to be heated until \dot{q}_{heat} terminates, and the temperature can rise well above $\mathcal{O}(10^6 \text{ K})$.

The DP-heating and radiative-cooling rates discussed above can be used to estimate several characteristic timescales relevant to our analysis. First, the injected energy density required to elevate the gas temperature to 3000 K at $r = 10^{15} \text{ cm}$ is $u_{\text{gas}} \simeq 10^{-4} \text{ erg cm}^{-3}$. At the same radius, the benchmark $(\varepsilon, m_{\gamma'})$ yields $\dot{q}_{\text{heat}} \simeq 4.1 \times 10^{-7} \text{ erg cm}^{-3} \text{ s}^{-1}$. The corresponding timescale to sublimate the dust, $t_{\text{sub}} \sim u_{\text{gas}}/\dot{q}_{\text{heat}} \simeq 243 \text{ s} \ll \bar{t}_{\text{dep}}$, is much shorter than the deposition duration \bar{t}_{dep} (see Fig. 4). The dust is thus destroyed rapidly, providing a substantial time window for the emission from the DP-induced photosphere to be constrained by Eq. (6). We also numerically verify that t_{sub} remains comparable along the lower red contour bounded by the solid black curve in Fig. 3.

At the same location, even after dust sublimation, DPs continue to deposit energy and heat the gas further until the temperature reaches $T_{\text{eq}} \simeq 12800 \text{ K}$, which only takes an additional $\sim 800 \text{ s}$. After reaching T_{eq} , the gas remains at T_{eq} for $\bar{t}_{\text{dep}} \simeq 9 \text{ hrs}$. A naive cooling-time estimate, $u_{\text{gas}}(T_{\text{eq}})/|\dot{q}_{\text{cool}}(T_{\text{eq}})|$, gives $\sim 0.3 \text{ hrs}$; however, because $|\dot{q}_{\text{cool}}|$ decreases as T drops, cooling from T_{eq} down to T_{sub} actually takes substantially longer. For instance, the time required for the temperature to fall from 6000 K to T_{sub} is approximately 50 hrs. Furthermore, even after the gas cools down to T_{sub} , the dust reformation requires additional time. As a result, we conclude

that dust does not reform to re-obscure the DP-heated photospheric emission over the time window relevant for comparison with the early non-detections.

Another key timescale is the radiative diffusion time through the optically-thick region inside r_{ph} , which approximately sets the duration of the DP-induced photospheric emission. For the benchmark case in Fig. 2, the average optical depth inside r_{ph} is $\bar{\tau} \simeq 17$, and it takes similar or larger values across the DP parameter space enclosed by the red contour in Fig. 3. The DP-induced photosphere emission duration is therefore expected to be $\bar{\tau} r_{\text{ph}}/c \gtrsim 20$ hrs.

Relevant early time observational data

Fig. 6 presents the amateur photometry data of SN 2023ixf reported to the TNS [108], where the 0d reference marks the initial report by K. Itagaki [82]. Instead of focusing on the brightness evolution corresponding to these early time data that involves complicated modeling [77, 112, 113], we utilize the three non-detections upper limits (colored triangles) before the earliest detection to constrain the DP heating as follows.

Assuming that the earliest detection at -0.87 d (MJD 60082.85) roughly traces the time when SN SBO from the stellar envelope at $r_s \simeq 5 \times 10^{13}$ cm [87] and taking a representative shock velocity $v_s \approx 8000$ km s $^{-1}$ [87] as the averaged shock speed during its propagation inside the progenitor, the corresponding SN core collapse can be estimated to happen at -1.58 d ($r_s/v_s \approx 17$ hrs) prior to detection. Accounting for the uncertainties due to the shock velocity ranging from $(8-10) \times 10^3$ km s $^{-1}$ [83, 87, 114] and the progenitor size from $(2.8-7) \times 10^{13}$ cm [87, 113, 115, 116], we estimate that core-collapse time may sit anywhere inside the gray band, roughly between -1.88 d to -1.19 d, shown in Fig. 6.

Since DPs produced after the core bounce arrive the CSM in ~ 1 hr and it takes $\lesssim 0.3$ hrs to heat up the CSM (see previous sections), the estimated ~ 20 hrs DP-induced photospheric emissions can be compared to the three upper limits between -1.56 d and -1.1 d: MJD 60082.25 (Kennedy [117]), MJD 60082.43 (ATLAS-o [118]), and MJD 60082.66 (XOSS [119]) to establish the constraint. The instrumentation for these observations includes a Sony IMX571 APS-C sensor (350–1050 nm, unfiltered) for the Kennedy observation and the ATLAS orange filter (560–820 nm) for ATLAS-o. The XOSS observation was conducted with a 0.2 m $f/7$ Schmidt-Cassegrain telescope. Although specific CMOS details were not documented for this epoch, we assume a spectral bandwidth comparable to the Sony IMX571 sensor. The band-limited absolute magnitude upper limits for all three non-detections are around $M \simeq -8.6$.

For simplicity, we adopt a representative bandpass of 400–900 nm to derive the band-limited luminosity L from

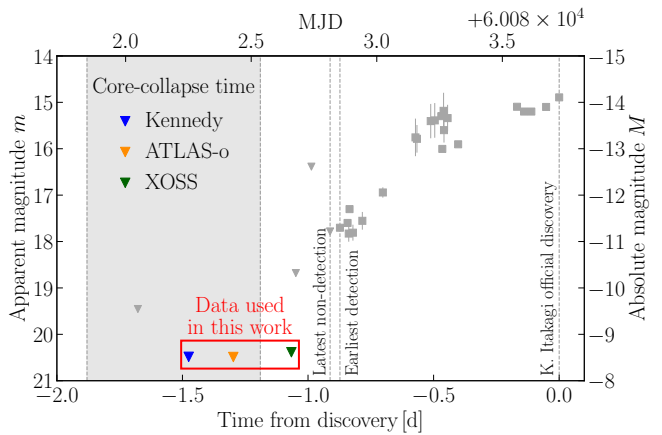


FIG. 6. Non-detection upper limits (triangles) and early-time detections (squares) of SN 2023ixf. The gray band indicates the estimated time interval when the core-collapse occurs. Colored triangles represent the data used to derive constraints in this study. Figure adapted from Ref. [120].

the corresponding band-limited absolute magnitude M by

$$\frac{L}{L_{\odot}} = 10^{0.4(M'_{\odot} - M)}, \quad (9)$$

where L'_{\odot} and M'_{\odot} are the solar luminosity and absolute magnitude in the same 400–900 nm range. L'_{\odot} and M'_{\odot} can be related to the solar luminosity L_{\odot} and absolute magnitude M_{\odot} across the full-wavelength range by

$$L'_{\odot} = \iota_{\odot} L_{\odot} \approx 2.03 \times 10^{33} \text{ erg s}^{-1}, \quad (10)$$

$$M'_{\odot} = M_{\odot} - 2.5 \log_{10} \iota_{\odot} \approx 5.41, \quad (11)$$

where $\iota_{\odot} = \iota(T_{\odot}) \approx 0.54$ for $T_{\odot} = 5772$ K, calculated by

$$\iota(T) = \frac{\int_{400 \text{ nm}}^{900 \text{ nm}} B_{\lambda}(T) d\lambda}{\int_0^{\infty} B_{\lambda}(T) d\lambda}, \quad (12)$$

which accounts for the fraction of the total power emitted within 400–900 nm for BB radiation with $B_{\lambda}(T)$ the corresponding Planck distribution. Using Eqs. (9)–(12) and taking $M \geq -8.6$ gives

$$L \leq 8.16 \times 10^{38} \text{ erg s}^{-1}. \quad (13)$$

To remain conservative and account for potential uncertainties in amateur photometry as well as other minor factors from galaxy dust extinction and red-shift corrections, we disfavor any DP parameters that produce a luminosity within 400–900 nm exceeding

$$\iota(T_{\text{ph}}) L_{\text{BB}}(\varepsilon, m_{\gamma'}) \leq 8 \times 10^{39} \text{ erg s}^{-1}, \quad (14)$$

which is almost a factor of 10 more stringent than Eq. (13).

Circumstellar Medium of Supernovae as New Probes for Feebly-interacting Particles

Supplemental Material

Yu Cheng, Chui-Fan Kong, Yen-Hsun Lin, Meng-Ru Wu, and Seokhoon Yun

In this supplementary, we use natural unit with $\hbar = c = 1$ for simplicity.

e^\pm energy spectrum from dark photon decay

Considering a dark photon (DP) that has mass $m_{\gamma'}$, energy ω , and momentum $k = |\mathbf{k}| = \sqrt{\omega^2 - m_{\gamma'}^2}$, its lab-frame velocity is $v = k/\omega$. In the DP rest frame, the two-body decay $\gamma' \rightarrow e^\pm$ is isotropic, and each e^\pm has fixed energy $m_{\gamma'}/2$. Let θ denote the relative angle between the e^\pm momentum \mathbf{p}_e in the DP rest frame and the boost direction \mathbf{v} . The lab-frame e^\pm energy follows from the Lorentz boost

$$E_{e,\theta} = \gamma \left(\frac{m_{\gamma'}}{2} + vp_e \cos \theta \right), \quad (\text{S1})$$

where $p_e = |\mathbf{p}_e| = \sqrt{m_{\gamma'}^2/4 - m_e^2}$ and $\gamma = \omega/m_{\gamma'}$. Integrating over the isotropic angular distribution (i.e., $\cos \theta$ is uniformly distributed in $[-1, 1]$), the lab-frame differential energy spectrum of the emitted electron/positron after is

$$\begin{aligned} \frac{dN_e}{dE_e}(\omega) &= \frac{1}{2} \int_{-1}^1 d \cos \theta \delta(E_e - E_{e,\theta}) \\ &= \frac{1}{2\gamma vp_e} \Theta(E_e - E_-) \Theta(E_+ - E_e), \end{aligned} \quad (\text{S2})$$

where $E_\pm = \gamma(m_{\gamma'}/2 \pm vp_e)$. The prefactor 1/2 arises from the isotropic two-body decay in the DP rest frame. Substituting dN_e/dE_e into dQ/dr given by Eq. (2) then yields the differential e^\pm luminosity deposited at radius r , per shell thickness dr and per e^\pm energy E_e .

Using Eq. (S2), we compute dQ/dr for the LS220-s18.88 model and show it as a function of r in Fig. S1 for representative values of $(\varepsilon, m_{\gamma'})$. After integrating over DP momentum, the result is approximately constant for $r \ll \bar{L}_d$ and exhibits an exponential falloff at $r \gtrsim \bar{L}_d$ due to the exponential decay factor e^{-r/L_d} . For example, the momentum-averaged DP decay length for $(\varepsilon, m_{\gamma'}) = (10^{-13}, 100 \text{ MeV})$ is $\bar{L}_d \simeq 6 \times 10^{15} \text{ cm}$.

Comparison of DP constraints from different EoS models

We investigate the sensitivity of the excluded DP parameter space to different nuclear equation of state (EoS) and progenitor mass by considering three representative models: SFHo-18.8 and LS220-s18.88 models from Ref. [97, 98], and the TF-10.8 from Ref. [121]. These

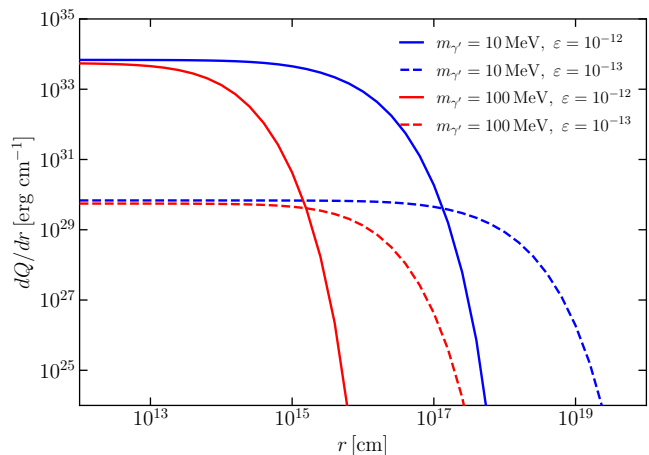


FIG. S1. The differential DP visible energy injection per unit radius dQ/dr as a function of r with the fiducial SN simulation model LS220-s18.88. Four cases corresponding to $\varepsilon = 10^{-12}$ and 10^{-13} as well as $m_{\gamma'} = 10$ and 100 MeV are shown.

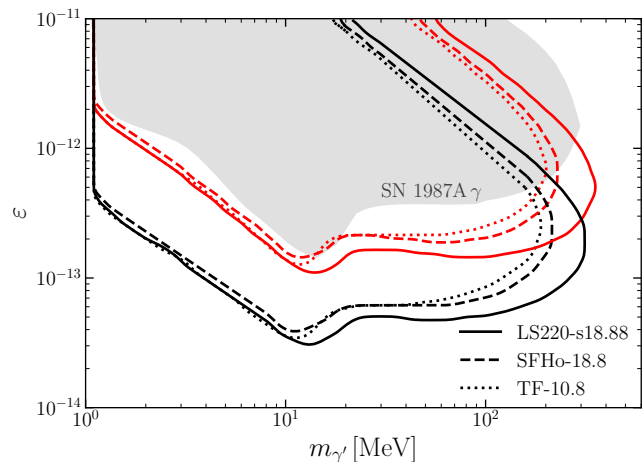


FIG. S2. The derived CSM-based constraints using different SN models: LS220-s18.88 (solid line), SFHo-18.8 (dashed line) and TF-10.8 (dotted line).

models primarily differ in the PNS temperature evolution, which controls the DP production rate and spectrum.

As shown in Fig. S2, the resulting constraints exhibit only modest model-to-model variation, with LS220-s18.88 yielding the strongest bound. We note that the prompt SN 1987A γ limit shown in the figure (adopted from Ref. [62]) was originally derived using

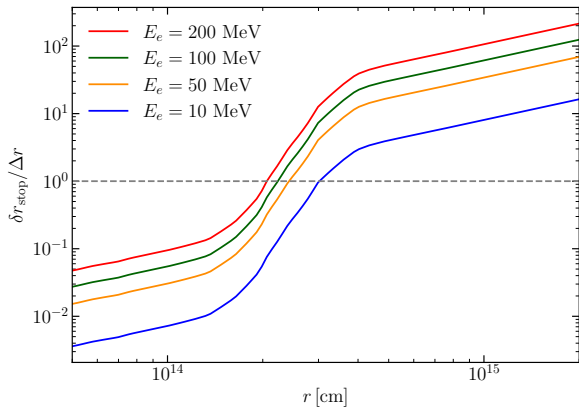


FIG. S3. The ratio of δr_{stop} to Δr as a function of r for various initial electron energies E_e . In the regions $r \lesssim 2 \times 10^{14}$ cm, the ratio remains below unity, indicating efficient energy deposition.

the LS220-s18.88 model. This limit (as well as other SN bounds) is therefore expected to carry a comparable degree of SN-model dependence as our CSM-based bounds. Even without accounting for that dependence explicitly, our CSM-based constraints remain stronger than the SN 1987A γ bound shown in Fig. S2, regardless of the choice of the SN model.

Electron energy loss after propagation

The energy loss per unit mass thickness for an electron (or positron) of energy E propagating through a medium of constant density ρ is characterized by the stopping power [99]

$$\mathcal{S}(E) = -\frac{1}{\rho} \frac{dE}{dx}, \quad (\text{S3})$$

where dE/dx is the energy loss per unit path length. In the medium with a uniform ρ , the propagation distance δr over which an electron cools from an initial energy E_e to a final energy E'_e reads

$$\delta r = \int_{E'_e}^{E_e} \frac{dE}{\rho \mathcal{S}(E)}. \quad (\text{S4})$$

Setting $E'_e = m_e$ defines the stopping length δr_{stop} .

Fig. S3 shows the ratio of the stopping length δr_{stop} to the shell thickness Δr . For simplicity, we take $\Delta r = r$, where r is the shell radius, and assume a uniform density ρ within the shell. Across the parameter space of interest, we find that for a broad range of initial energies E_e , the stopping length remains smaller than the shell thickness for $r \lesssim 2 \times 10^{14}$ cm, implying a deposition efficiency $\eta \simeq 1$. When $\delta r_{\text{stop}} > \Delta r$, we truncate the stopping length at $\delta r_{\text{stop}} = \Delta r$ and determine the corresponding energy E'_e from Eq. (S4) numerically, resulting in a reduced deposition efficiency.

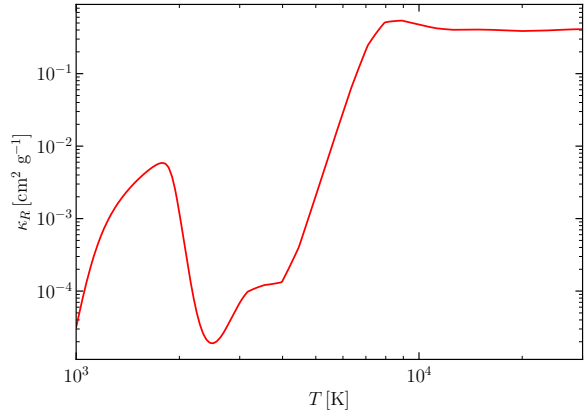


FIG. S4. The Rosseland mean opacity κ_R as a function of temperature, assuming $\rho \approx 2 \times 10^{-12}$ g cm $^{-3}$.

Opacity

To evaluate the optical depth τ , we adopt the Rosseland mean opacity κ_R from the Ferguson [104] and OPAL [103] tables for $T < 10^4$ K and $T \geq 10^4$ K, respectively. Assuming a medium density of $\rho \approx 2 \times 10^{-12}$ g cm $^{-3}$, which is the mean value in the dense regime, Fig. S4 shows κ_R as a function of temperatures. The steep rise of κ_R for $T \gtrsim 5000$ K, approaching $\gtrsim 0.1$ cm 2 g $^{-1}$, is related to efficient H $^-$ formation. This increase in opacity is the main reason that photon-trapping becomes efficient in the inner CSM heated by DP decays.